Article

Perovskite superlattices with efficient carrier dynamics

Check for updates

Yusheng Lei[1,2,11], Yuheng Li[1,11], Chengchangfeng Lu[3], Qizhang Yan[1], Yilei Wu[2], Finn Babbe[4], Huaxin Gong[2], Song Zhang[2], Jiayun Zhou[5], Ruotao Wang[1], Ruiqi Zhang[1], Yimu Chen[1], Hsinhan Tsai[6], Yue Gu[5], Hongjie Hu[1], Yu-Hwa Lo[3], Wanyi Nie[6], Taeyoon Lee[7,8], Jian Luo[1,5], Kesong Yang[1], Kyung-In Jang[9] & Sheng Xu[1,5,6,10 ✉]

Compared with their three-dimensional (3D) counterparts, low-dimensional metal halide perovskites (2D and quasi-2D; $B_2A_{n-1}M_nX_{3n+1}$, such as $B = R\text{-}NH_3^+$, $A = HC(NH_2)_2^+$, Cs^+; $M = Pb^{2+}$, Sn^{2+}; $X = Cl^-$, Br^-, I^-) with periodic inorganic–organic structures have shown promising stability and hysteresis-free electrical performance[1–6]. However, their unique multiple-quantum-well structure limits the device efficiencies because of the grain boundaries and randomly oriented quantum wells in polycrystals[7]. In single crystals, the carrier transport through the thickness direction is hindered by the layered insulating organic spacers[8]. Furthermore, the strong quantum confinement from the organic spacers limits the generation and transport of free carriers[9,10]. Also, lead-free metal halide perovskites have been developed but their device performance is limited by their low crystallinity and structural instability[11]. Here we report a low-dimensional metal halide perovskite $BA_2MA_{n-1}Sn_nI_{3n+1}$ (BA, butylammonium; MA, methylammonium; $n = 1, 3, 5$) superlattice by chemical epitaxy. The inorganic slabs are aligned vertical to the substrate and interconnected in a criss-cross 2D network parallel to the substrate, leading to efficient carrier transport in three dimensions. A lattice-mismatched substrate compresses the organic spacers, which weakens the quantum confinement. The performance of a superlattice solar cell has been certified under the quasi-steady state, showing a stable 12.36% photoelectric conversion efficiency. Moreover, an intraband exciton relaxation process may have yielded an unusually high open-circuit voltage (V_{OC}).

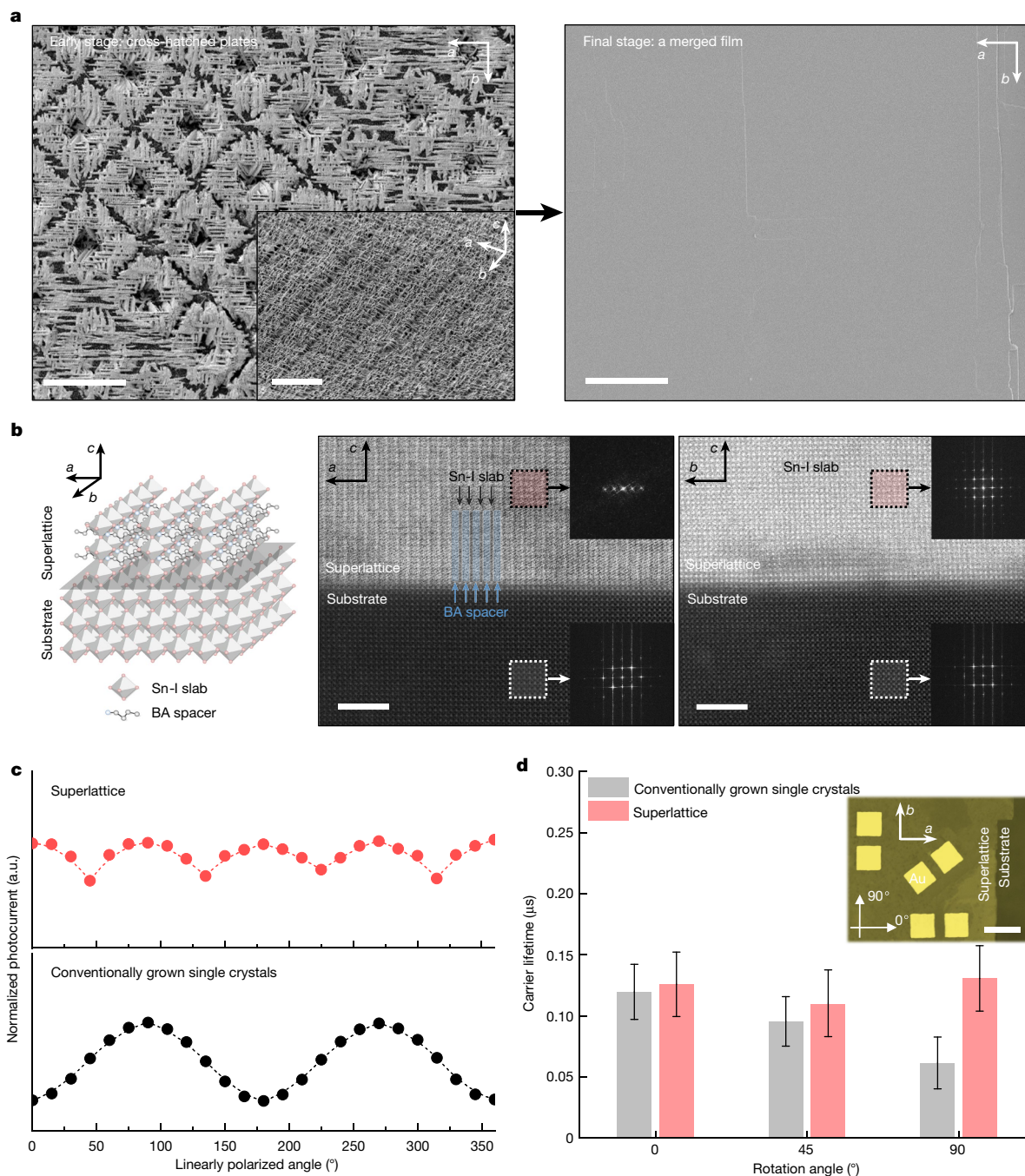We studied the growth process and structure of BA_2SnI_4 ($n = 1$) super-lattice on a $MAPb_{0.5}Sn_{0.5}Br_3$ substrate (Supplementary Discussion 1 and Supplementary Figs. 1–4). The Sn-I slabs exhibit a favourable epitaxial relationship with the substrate, forming a thermodynamically stable, vertically aligned lattice[12] (Supplementary Fig. 1). Scanning electron microscopy (SEM) images show that the crystals first grow into criss-cross vertical thin plates followed by lateral merging (Fig. 1a and Supplementary Fig. 2). Similar growth behaviour can be observed in other low-dimensional perovskites grown on different substrates (Supplementary Figs. 3 and 5). Cryogenic scanning transmission electron microscopy (STEM) was used to study the structure of a single plate, which exhibits anisotropy (Fig. 1b). The a–c plane shows a periodic distribution of inorganic Sn-I slabs and organic BA spacers along the a direction (Fig. 1b, middle and Supplementary Fig. 6). The b–c plane shows a continuous Sn-I slab with a coherent heteroepitaxial interface with the substrate (Fig. 1b, right). Therefore, the criss-cross vertical plates on the substrates create a 3D network of Sn-I slabs, not seen previously in any polycrystals (Supplementary Fig. 7) or conventionally grown single

crystals. Furthermore, grazing-incidence wide-angle X-ray scattering further verified their vertically aligned structures[13,14] (Supplementary Fig. 8).

To further study the crystal orientation in the a–b plane, we measured the polarization-dependent photocurrent of superlattices and conventionally grown single crystals (Fig. 1c). The results in both show a strong dependence on the polarization direction, but the response of superlattices has a 90° period, whereas that of conventionally grown single crystals has a 180° period. This is because the inorganic slabs are aligned in two perpendicular orientations in the a–b plane of super-lattices, but in only one orientation of conventionally grown single crystals (Supplementary Fig. 9). Similar trends can also be observed in the carrier lifetime obtained from orientation-dependent transient photovoltage measurements (Fig. 1d and Supplementary Fig. 10). These results collectively support that the superlattice has Sn-I slabs intercon-nected, with numerous criss-cross thin plates merged in the a–b plane.

Because of the interconnected Sn-I slabs, carriers in the superlattice do not need to cross any grain boundaries or organic spacers both in plane and out of plane. Transient photocurrent measurements along

[1]Department of Nanoengineering, University of California, San Diego, La Jolla, CA, USA. [2]Department of Chemical Engineering, Stanford University, Stanford, CA, USA. [3]Department of Electrical and Computer Engineering, University of California, San Diego, La Jolla, CA, USA. [4]Chemical Sciences Division, Liquid Sunlight Alliance, Lawrence Berkeley National Laboratory, Berkeley, CA, USA. [5]Materials Science and Engineering Program, University of California, San Diego, La Jolla, CA, USA. [6]Los Alamos National Laboratory, Los Alamos, NM, USA. [7]School of Electrical and Electronic Engineering, Yonsei University, Seoul, Republic of Korea. [8]Department of Bio and Brain Engineering, Korea Institute of Science and Technology, Seoul, Republic of Korea. [9]Department of Robotics Engineering, Daegu Gyeongbuk Institute of Science and Technology, Daegu, Republic of Korea. [10]Department of Bioengineering, University of California, San Diego, La Jolla, CA, USA. [11]These authors contributed equally: Yusheng Lei, Yuheng Li. ✉e-mail: shengxu@ucsd.edu
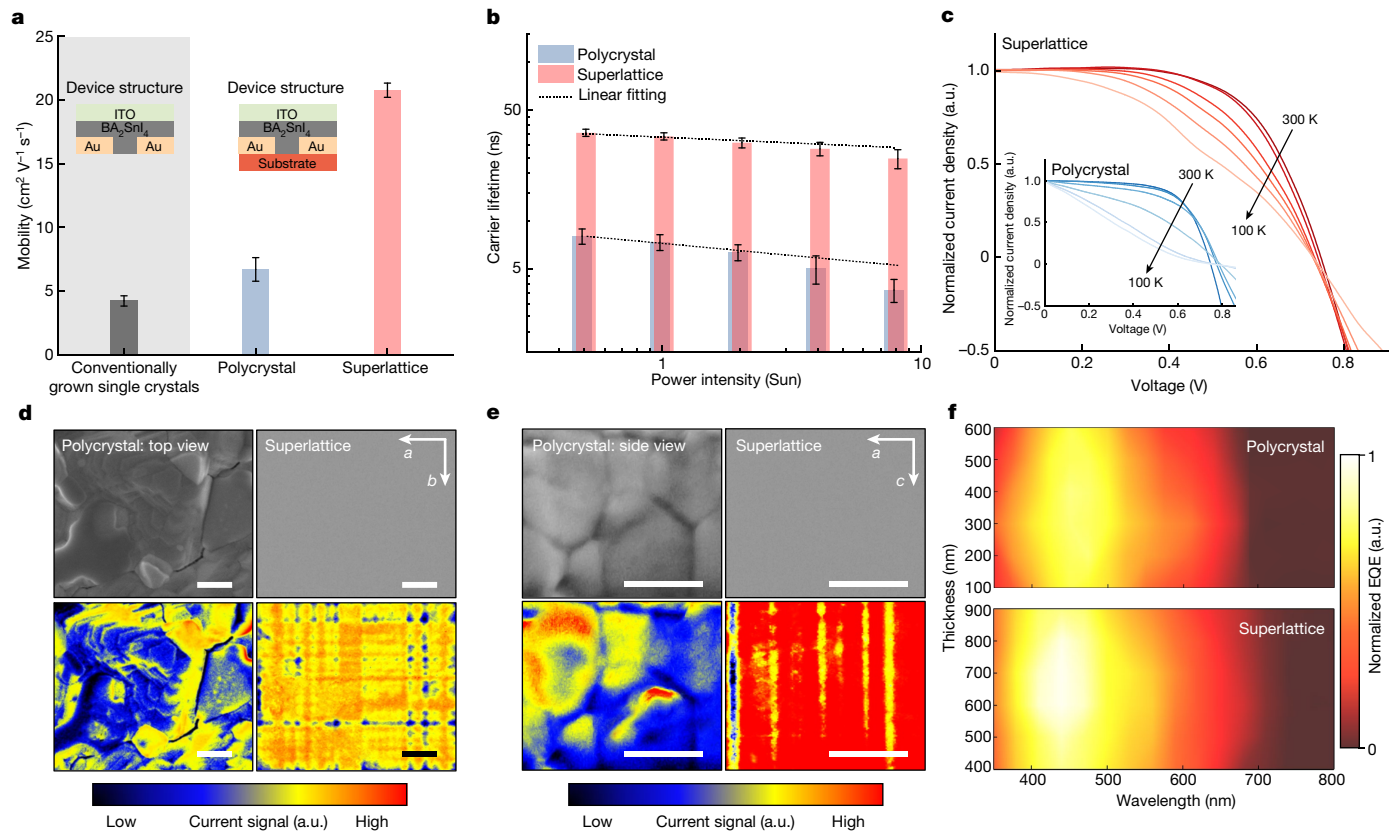
Fig. 1 | Structural characterizations of the BA₂SnI₄ superlattice. a, SEM images showing the criss-cross epitaxial BA_2SnI_4 superlattice before and after merging into a thin film. Scale bars, 2 μm. **b**, Schematic (left) and atomic-resolution cryogenic STEM images (middle and right) showing the superlattice structure of a single plate. Cryogenic STEM is essential to minimize the damage of beam-sensitive materials. The epitaxial layer has a well-aligned anisotropic structure without grain boundaries or dislocations. The insets are fast Fourier transform patterns from the epitaxial layer in the a–c plane, which show a 2D diffraction pattern of the superlattice and is different from that of the substrate (middle). The inset fast Fourier transform images in the b–c plane show the structural similarity between the inorganic slab and the substrate (right). Organic atoms are usually invisible under electron diffraction. Scale bars, 6 nm. **c**, Photocurrent measurements with a linearly polarized excitation source showing that the response of the epitaxial layer (top) shows a period that is half of that of a conventionally grown single crystal (bottom). **d**, Transient photovoltage measurements showing the orientation-dependent carrier lifetime in the a–b plane. The inset optical image shows the measurement setup. The error bars are from measurements of five different devices. Scale bar, 500 μm.

the film thickness (c direction) show a much higher carrier mobility in the superlattice than in the polycrystalline or conventionally grown single-crystal sample (Fig. 2a). The grain boundaries in polycrystals markedly reduce carrier mobility[15] (Supplementary Fig. 11). The layered organic spacers make the mobility in conventionally grown single crystals the lowest (Supplementary Fig. 12). Power-dependent time-resolved photoluminescence measurements show that the superlattice has a longer carrier lifetime than the polycrystal (Fig. 2b), indicating minimal restriction of the carriers. Furthermore, superlattices show better tolerance to high excitation power than polycrystals, suggesting that better crystallinity can reduce material degradation under high excitation power[16].

Fig. 2 | Carrier transport properties of the BA$_2$SnI$_4$ superlattice. a, Transient photocurrent measurements along the film thickness (*c*) direction. The superlattice shows the highest carrier mobility. The carrier mobility in the polycrystal is limited by grain boundaries and lattice misalignments between grains. The conventionally grown single crystal shows the lowest carrier mobility because of the energy barriers caused by the organic spacers along the film thickness direction. The insets show the schematic measurement setups. The error bars are from measurements of five different devices. **b**, Time-resolved photoluminescence measurements showing a longer carrier lifetime in the superlattice than the polycrystal. The lifetime–power relationship in the polycrystal tends to deviate from a linear fit (dashed lines) at high excitation power owing to absorber degradation. The error bars are from measurements of five different devices. **c**, Temperature-dependent *J–V* measurements on solar cells (ITO/ICBA/perovskite/PTAA/Au; active size, 1 mm^2) fabricated on as-grown films. The current density values are

normalized. As temperature drops, the FF of the superlattice device does not change as strongly as the polycrystal device, indicating a lower internal energy barrier in the superlattice. PTAA, poly[bis(4-phenyl)(2,4,6-trimethylphenyl) amine]. **d**, SEM images and corresponding EBIC mapping of the top surface of BA$_2$SnI$_4$ films. The polycrystal exhibits grain-dependent current signals. The superlattice exhibits stronger current signals with a criss-cross pattern, even with a smooth film surface. Scale bars, 200 nm. **e**, SEM images and corresponding EBIC mapping of the cross section of BA$_2$SnI$_4$ films. The polycrystal exhibits grain-dependent current signals. The superlattice exhibits stronger current signals with a linear pattern. Scale bars, 100 nm. **f**, Thickness-dependent EQE measurements. The superlattice device exhibits a higher EQE with a larger optimal absorber thickness, indicating that the carrier diffusion length in the superlattice is longer than that in the polycrystal. A longer-wavelength collection edge also indicates a smaller bandgap in the superlattice.
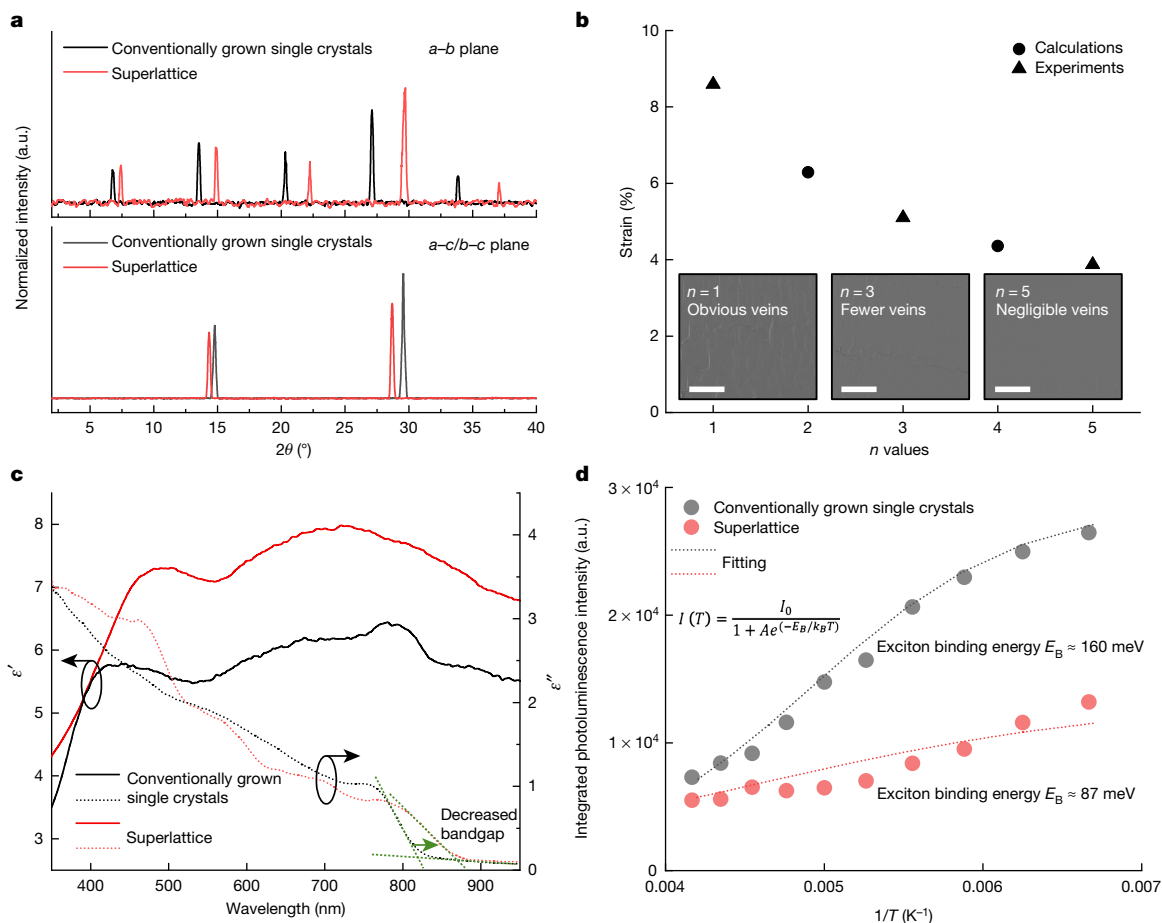
The structural advantages of superlattices are validated with temperature-dependent current density–voltage (*J–V*) characteristics of a BA$_2$SnI$_4$ solar cell. To investigate internal energy barrier for carrier transport, we fabricated a device directly on the superlattice without peeling it off from the epitaxial substrate to minimize any possible confounding factors introduced by the fabrication process[15] (Supplementary Discussion 2 and Supplementary Figs. 13 and 14). As the temperature gradually decreases, thermal energy becomes too small for the carriers to overcome barriers (for example, owing to ionized impurity scattering), so the fill factor (FF) decreases substantially for both superlattice and polycrystalline devices (Fig. 2c). However, the decrease is less pronounced in superlattices, indicating lower internal energy barriers.

We measured the electron-beam-induced current (EBIC) to visualize carrier transport barriers. For polycrystals, the collected currents on the thin film surface heavily depend on grain orientations, indicating disorientated multiple quantum wells (Fig. 2d, left). By contrast, superlattices yield higher and much more uniform currents owing to the well-aligned crystal structure (Fig. 2d, right). Note that superlattices

exhibit a criss-cross current pattern owing to their imperfect merging during solution growth (Supplementary Fig. 15). Similar observations can also be made in the sample cross sections (Fig. 2e and Supplementary Discussion 3).

The improved carrier dynamics of superlattices allows a longer carrier diffusion length. As the photovoltaic absorber, the thickness of polycrystals is usually highly restricted[17], for which the external quantum efficiency (EQE) peaks at about 400 nm for BA$_2$SnI$_4$ (Fig. 2f, top). By contrast, the absorber thickness for superlattices can be increased to around 700 nm with enhanced light absorption and, thus, EQE (Fig. 2f, bottom).

We investigated the heteroepitaxial strain in BA$_2$SnI$_4$ superlattices quantitatively by X-ray diffraction. Compared with conventionally grown single crystals, high overall compressive strains are present in superlattices along the *a* and *b* directions, at around 8.59% and around 1.32%, respectively (Fig. 3a, top); a tensile strain of roughly 0.99% is present in the *c* direction owing to the Poisson effect[18] (Fig. 3a, bottom, Supplementary Discussion 4 and Supplementary Table 1). These strains are validated by STEM images (Supplementary Fig. 6 and Supplementary
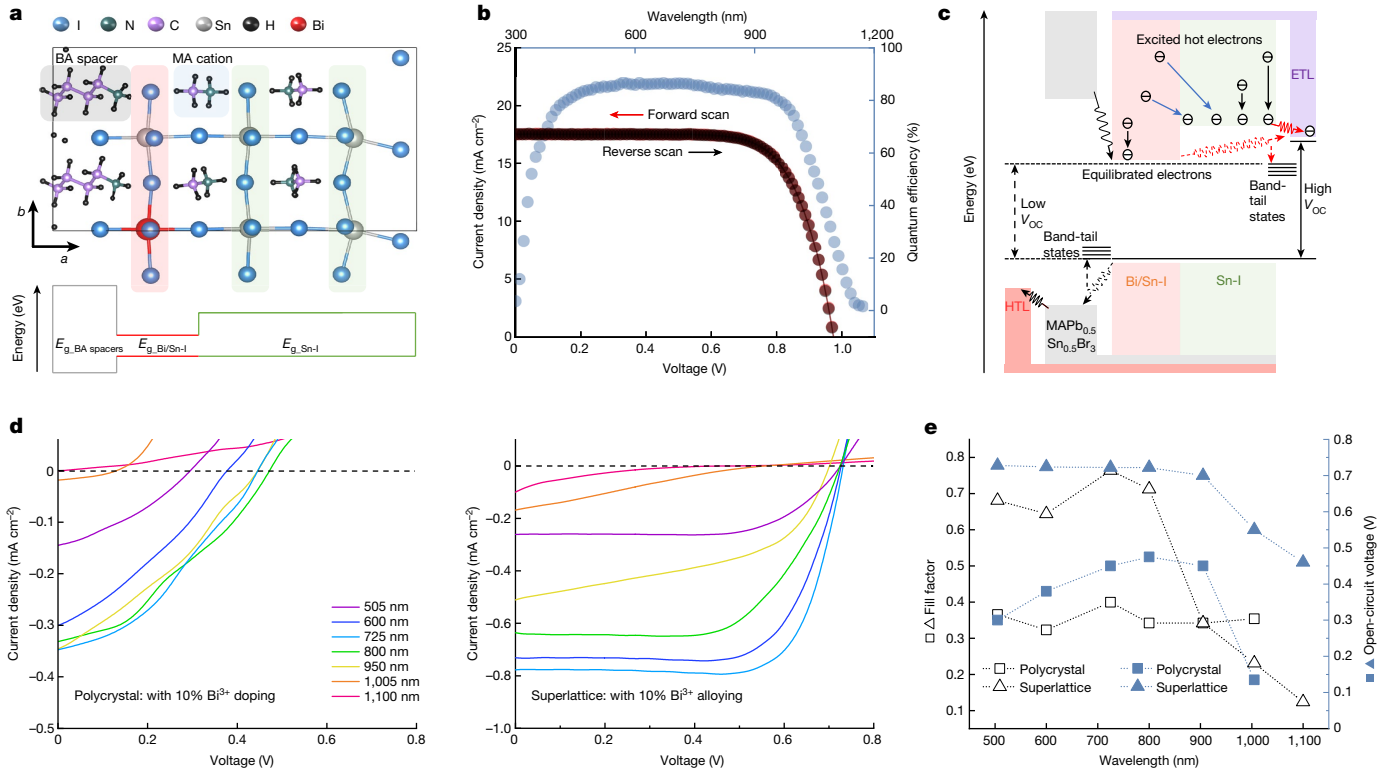
Fig. 3 | Strain properties of BA$_2$MA$_{n-1}$Sn$_n$I$_{3n+1}$ superlattices. a, X-ray diffraction measurements of the BA$_2$SnI$_4$ superlattice and conventionally grown BA$_2$SnI$_4$ single crystals. A compressive strain in the a–b plane and a tensile strain along the c direction are observed in the superlattice. **b**, DFT-computed and experimentally calculated lattice strain with different n in low-dimensional BA$_2$MA$_{n-1}$Sn$_n$I$_{3n+1}$ perovskites. Crystals with larger n will have smaller strain. Inset SEM images show that a larger n will result in a smoother surface, which is attributed to fewer defects under smaller epitaxial strain. Scale bars, 50 μm. **c**, Ellipsometry measurements of the dielectric function ($\varepsilon' + i\varepsilon''$) of the BA$_2MA_2Sn_3I_{10}$ superlattice and conventionally grown BA$_2$MA$_2$Sn$_3$I$_{10}$ single crystals. The larger ε' in the superlattice indicates that the

compressive strain can increase the dielectric constant and the Bohr radius in the superlattice. A red shift in ε'' shows that the compressive strain decreases the bandgap of the superlattice. **d**, Estimated exciton binding energies obtained from temperature-dependent photoluminescence measurements. The smaller fitted exciton binding energy in the superlattice than the polycrystal indicates a weaker quantum confinement effect because of the smaller width of the organic barrier. In the inset equation, I is the integrated photoluminescent intensity, I_0 is the integrated intensity at room temperature, A is an arbitrary constant, E_B is the exciton binding energy, k_B is the Boltzmann constant and T is the temperature.

Discussion 4). Structural computation by density functional theory (DFT) further shows a lattice compression of Sn-I slabs from about 6.04 Å to about 5.94 Å in the a direction (Supplementary Fig. 16), yielding an approximately 1.66% strain, which is close to the 1.32% strain in the b direction; the width of organic spacers is compressed from about 7.00 Å to about 5.98 Å (Supplementary Figs. 16 and 17), corresponding to an approximately 14.6% strain. Therefore, the high compressive strain is mostly accommodated by organic spacers. High strain reduces the stability of superlattices (Supplementary Figs. 18 and 19). For general heteroepitaxial BA$_2$MA$_{n-1}$Sn$_n$I$_{3n+1}$, as n increases, the volume ratio of the Sn-I slabs increases, the overall lattice strain decreases (Fig. 3b) and the structure is more stable. Moreover, lower strain results in fewer structural defects and smoother surfaces (Fig. 3b, inset images).

To avoid structural change and achieve reliable measurements of superlattices, we chose BA$_2$MA$_2$Sn$_3$I$_{10}$ ($n = 3$) to study their strain-controlled optoelectronic properties. We used ellipsometry to study the dielectric functions ($\varepsilon' + i\varepsilon''$). The higher ε' of superlattices indicates weakened quantum confinement by compressed organic spacers (Fig. 3c), a larger Bohr radius in the multiple quantum wells and, therefore, a higher rate of free-carrier generation[19] (Supplementary

Discussion 5). Besides, the shift in ε'', which reflects the absorption wavelength[20], suggests a smaller bandgap in superlattices compared with conventionally grown single crystals, which is also evident by the longer-wavelength collection edge of superlattices (Fig. 2f and Supplementary Fig. 20). Temperature-dependent photoluminescence measurements also show a much-reduced fitted exciton binding energy in superlattices compared with conventionally grown single crystals[18,19] (Fig. 3d). In addition, the carrier lifetime in superlattices is slightly longer than conventionally grown single crystals at 0° in transient photovoltage measurements (Fig. 1d). All these characteristics can be attributed to the weakened quantum confinement in superlattices.

Large heteroepitaxial strains heavily influence the stability of superlattices (Fig. 3b, Supplementary Discussion 4 and Supplementary Figs. 18 and 19). We choose BA$_2$MA$_4$Sn$_5$I$_{16}$ ($n = 5$) to investigate the device performance owing to its better stability. To further relieve the strain and create an even more stable structure, we investigated using Bi^{3+} (103 pm in radius[21]) to partially replace Sn^{2+} (118 pm in radius[22]). DFT calculations show that the Bi^{3+} tends to concentrate at the interface between the inorganic slab and the organic spacer to relieve the compressive strain (Fig. 4a, top and Supplementary Fig. 21), forming an aggregated
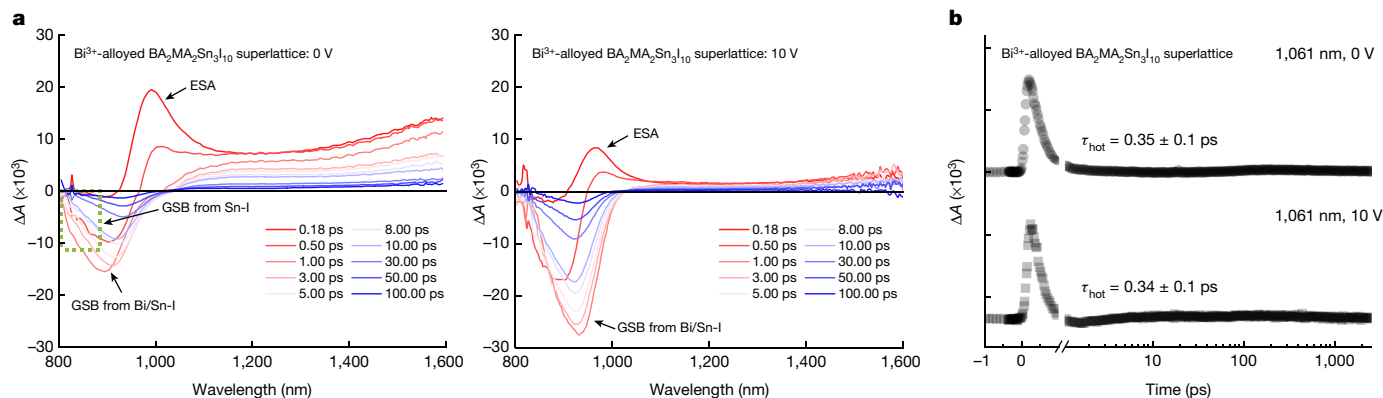
Fig. 4 | Photovoltaic studies of Bi³⁺-alloyed superlattice. a, Structure of the Bi³⁺-alloyed $BA_2MA_2Sn_3I_{10}$ superlattice computed by DFT. The Bi³⁺ ions preferentially aggregate at the interface between the organic and inorganic slabs to relieve the lattice strain (top). The aggregated Bi³⁺ alloying alters the electronic band structure, resulting in a substantially decreased CBM. Combined with the region without Bi³⁺, they form a double-band structure in the inorganic slab (bottom). **b**, Certified photovoltaic performance measurement based on a Bi³⁺-alloyed $BA_2MA_4Sn_5I_{16}$ superlattice, showing a bandgap of 1.042 eV and a V_{OC} of 0.967 V. **c**, Unusual carrier transport processes with intraband relaxation, resulting in a high V_{OC}. Note that both Sn-I and Bi/Sn-I regions are in direct physical contact with the ETL. HTL, hole transport layer.

d, Wavelength-dependent J–V measurements of a polycrystalline solar cell with a uniform Bi³⁺ distribution and, therefore, a single bandgap (left) and a superlattice (right) solar cell. In the polycrystalline device, reasonably small variations in the FF indicate that the carrier transport and the collection are almost independent of wavelength; therefore, the abruptly decreased V_{OC} at about 1,000 nm suggests that the uniform Bi³⁺ distribution does not alter the band structure. In the superlattice device, when the incident wavelength is shorter than around 900 nm, neither FF nor V_{OC} exhibit an obvious wavelength dependency. However, once the excitation wavelength is longer than about 900 nm, both FF and V_{OC} decrease substantially. **e**, Extracted FF and V_{OC} from **d**.

Bi³⁺ atomic layer to decrease the formation energy (Supplementary Fig. 22 and Supplementary Discussion 6) of the superlattice and yield a more stable structure (Supplementary Fig. 23). Furthermore, the aggregated Bi³⁺ alloying decreases the conduction band minimum (CBM) (Fig. 4a, bottom and Supplementary Figs. 24 and 25). The region without Bi³⁺ alloying remains intact. The result is an inorganic slab with a double-band structure.

We studied the photovoltaic performance of those superlattices. We chose 10% Bi³⁺-alloyed $BA_2MA_4Sn_5I_{16}$ ($n = 5$) superlattice with a textured surface and fabricated a solar cell directly on the epitaxial substrate (Supplementary Figs. 26 and 27). Indene-C60 bisadduct (ICBA) was used as the electron transport layer (ETL) because its CBM level (Supplementary Fig. 28) is higher than that of the Bi/Sn-I but lower than the Sn-I slabs (Supplementary Table 2). The Bi/Sn-I and the Sn-I regions are both in contact with the ETL. The as-certified superlattice solar cell exhibits a stable 12.36% photoelectric conversion efficiency under the quasi-steady state (Supplementary Fig. 29)—the highest in lead-free low-dimensional perovskite solar cells. To further replace the lead-containing substrate, it is also feasible to use other substrates (Supplementary Figs. 3 and 5) or to exfoliate and transfer the superlattice from the epitaxial substrate to a general substrate (Supplementary Figs. 30, 31 and 32). Moreover, the quantum efficiency of the solar cell (Fig. 4b and Supplementary Fig. 29) shows a carrier collection cut-off at approximately 1,190 nm, which gives a bandgap of about 1.042 eV

and a V_{OC} of at most 0.802 V according to the Shockley–Queisser limit[23]. However, the certified V_{OC} is 0.967 V, indicating other contributing mechanisms.

Figure 4c shows the schematic band diagram of the superlattice solar cell. Because the aggregated Bi³⁺ alloying in superlattices could lead to a radiative band structure besides the band-tail states that commonly exist in Bi³⁺-doped polycrystals[24–29] (Supplementary Fig. 23 and Supplementary Discussion 6), an intraband relaxation mechanism is possible for contributing to the high V_{OC}. We performed wavelength-dependent J–V measurements to investigate the potential mechanism (Fig. 4d,e). Under short incident wavelengths (less than about 1,000 nm), most electrons are excited into energy states higher than the CBM of both Sn-I and Bi/Sn-I regions. Those electrons from the Sn-I region naturally relax to the CBM of the Sn-I region. Furthermore, a substantial portion of the electrons from the Bi/Sn-I region can also relax to the CBM of the Sn-I region through intraband relaxation (solid blue arrows in Fig. 4c). This transition is possible because the atomic-thin Bi/Sn-I region is easy for carriers to diffuse across. Also, the built-in potential in the p-i-n structure might have facilitated this atomic-scale transition; moreover, the ETL layer favours electron collection from the Sn-I region (solid red arrow in Fig. 4c). Therefore, most of the carriers are in the Sn-I region, yielding a high V_{OC} and a high FF (Fig. 4d,e). Under long incident wavelengths (more than about 1,000 nm), electrons can only be excited in the Bi/Sn-I region. The relatively low-energy

Fig. 5 | Dynamics analysis of hot electrons in Bi³⁺-alloyed superlattices. **a**, Measured transient absorption spectra for Bi³⁺-alloyed BA₂MA₂Sn₃I₁₀ superlattice devices. It is clear to see that the device exhibits obvious changes in GSB and ESA intensities with and without the 10-V bias, suggesting bias-dependent hot carrier dynamics in Bi³⁺-alloyed BA₂MA₂Sn₃I₁₀ superlattice devices. **b**, Extracted hot carrier relaxation lifetimes from **a** for Bi³⁺-alloyed BA₂MA₂Sn₃I₁₀ superlattice devices. Their lifetimes show negligible changes with and without the 10-V bias, excluding the influence of the applied bias on the hot carrier lifetimes.

electrons can only relax to the CBM of the Bi/Sn-I region and then to the ETL by means of interband transition (dashed red arrows in Fig. 4c). Therefore, most of the carriers are in the Bi/Sn-I region, contributing to a low V_{OC} (Fig. 4d,e). The energy barrier between the Bi/Sn-I region and the ETL causes serious charge accumulation (Supplementary Discussion 7), resulting in a low FF (Fig. 4d,e). When the device is excited under mixed incident wavelengths, the high-energy electrons facilitate the quasi-Fermi-level splitting in the Sn-I region. The low-energy electrons will have a relatively small influence on the overall V_{OC} because of the small portion of long wavelengths (between about 1,000 nm and about 1,200 nm) in the solar spectrum (roughly 9%)[30] and, thus, the small quantity of the low-energy electrons. The overall V_{OC} is predominantly determined by the bandgap of the Sn-I region (Supplementary Fig. 33 and Supplementary Discussion 7).

To verify this mechanism, we collected pump–probe ultrafast transient absorption spectra to investigate their hot carrier dynamics (Supplementary Discussion 8). To meet the measurement requirement, a transferred device structure (ITO/superlattice/ICBA/polypropylene tape/ITO) (Supplementary Fig. 34) was adopted under an external electrical field to mimic the built-in potential of the solar cell. We measured transient absorption spectra with and without the bias (Fig. 5a and Supplementary Figs. 35 and 36). The polycrystalline thin films exhibit very different spectral profiles from superlattices (Fig. 5a and Supplementary Fig. 35). Obvious ground state bleaching (GSB) signals in the negative intensity region could only be observed in superlattices, indicating more efficient carrier dynamics in the superlattices than those in the polycrystalline thin films.

The lifetime of hot electrons could be obtained by extracting and fitting relaxation time profiles at selected wavelengths (Fig. 5b and Supplementary Fig. 37). The hot electron lifetimes of superlattices (Bi³⁺-alloyed and Bi³⁺-free) are between about 0.35 and 0.36 ps, which are almost twice that of Bi³⁺-doped polycrystalline thin films (approximately 0.19 ps) (Supplementary Fig. 37). Accordingly, the calculated hot electron diffusion length in superlattices is around 3.9 nm, much longer than the width of the Bi/Sn-I regions (about 0.6 nm) (Supplementary Fig. 37), suggesting that the hot electrons can readily travel across the Bi/Sn-I regions to the Sn-I regions. Furthermore, transient absorption spectra show an obviously enhanced GSB intensity in Bi³⁺-alloyed superlattices when the applied bias increases from 0 V to 10 V (Fig. 5a). By contrast, the excited state absorption (ESA) signal decreases (Fig. 5a). However, no such phenomenon can be observed in Bi³⁺-free superlattices or Bi³⁺-doped polycrystalline thin films (Supplementary Fig. 35), supporting the potential intraband relaxation in Bi³⁺-alloyed superlattices: the increased GSB signal intensity indicates

a reduced number of electrons at the ground state in the valence band. Because the excitation setups for 0-V and 10-V measurements are the same, the reduced electrons at the ground state in the valence band are not from a stronger excitation. Therefore, it suggests that the number of electrons relaxing from the conduction band to the valence band after excitation is reduced. However, because the hot carrier lifetime is minimally influenced by the electrical field (Fig. 5b and Supplementary Figs. 37 and 38), those 'reduced' electrons can only transport to Sn-I regions but not to the ITO or ICBA layers because of the direction of the applied electrical field and the strong interfacial barriers, respectively (Supplementary Discussion 8).

The decreased ESA intensities owing to a reduced number of hot electrons in the valence band provide further evidence for the potential intraband relaxation. However, because of the same excitation setup and similar hot electron lifetimes for 0-V and 10-V measurements (Fig. 5b and Supplementary Figs. 37 and 38), the obviously reduced hot electron population is not from a weaker excitation or more rapid relaxation but from other relaxation routes. The excited hot electrons have short lifetimes and can only undergo atomic-scale diffusion to Sn-I regions but not to the ITO or ICBA layers (Supplementary Discussion 8).

Besides the unique intraband relaxation mechanism discussed here, other carrier transport processes might also be possible for the high V_{OC}, such as the superposition principles between parallel subcells[31], sub-band absorption[32], multiple exciton generation in atomic-scale structures[33] and ion diffusions[34]. Further research is required to gain a complete understanding of this phenomenon. Continued improvements in the device performance are possible with optimizations of the design of the electrode patterns, the resistivity of the top electrode and the band alignment of the ETL/hole transport layer.

Online content

Any methods, additional references, Nature Research reporting summaries, source data, extended data, supplementary information, acknowledgements, peer review information; details of author contributions and competing interests; and statements of data and code availability are available at https://doi.org/10.1038/s41586-022-04961-1.

1. Zhang, W., Eperon, G. E. & Snaith, H. J. Metal halide perovskites for energy applications. *Nat. Energy* **1**, 16048 (2016).
2. de Arquer, F. P. G., Armin, A., Meredith, P. & Sargent, E. H. Solution-processed semiconductors for next-generation photodetectors. *Nat. Rev. Mater.* **2**, 16100 (2017).
3. Lei, Y., Chen, Y. & Xu, S. Single-crystal halide perovskites: opportunities and challenges. *Matter* **4**, 2266–2308 (2021).

4. Park, N. G. Research direction toward scalable, stable, and high efficiency perovskite solar cells. *Adv. Energy Mater.* **10**, 1903106 (2020).
5. Blancon, J.-C. et al. Extremely efficient internal exciton dissociation through edge states in layered 2D perovskites. *Science* **355**, 1288–1292 (2017).
6. Qin, C. et al. Stable room-temperature continuous-wave lasing in quasi-2D perovskite films. *Nature* **585**, 53–57 (2020).
7. Grancini, G. & Nazeeruddin, M. K. Dimensional tailoring of hybrid perovskites for photovoltaics. *Nat. Rev. Mater.* **4**, 4–22 (2019).
8. Liu, Y. et al. Surface-tension-controlled crystallization for high-quality 2D perovskite single crystals for ultrahigh photodetection. *Matter* **1**, 465–480 (2019).
9. Blancon, J.-C. et al. Scaling law for excitons in 2D perovskite quantum wells. *Nat. Commun.* **9**, 2254 (2018).
10. Gélvez-Rueda, M. C. et al. Overcoming the exciton binding energy in two-dimensional perovskite nanoplatelets by attachment of conjugated organic chromophores. *Nat. Commun.* **11**, 1901 (2020).
11. Ke, W. & Kanatzidis, M. G. Prospects for low-toxicity lead-free perovskite solar cells. *Nat. Commun.* **10**, 965 (2019).
12. Soe, C. M. M. et al. Structural and thermodynamic limits of layer thickness in 2D halide perovskites. *Proc. Natl Acad. Sci. USA* **116**, 58–66 (2019).
13. Chen, A. Z. et al. Origin of vertical orientation in two-dimensional metal halide perovskites and its effect on photovoltaic performance. *Nat. Commun.* **9**, 1336 (2018).
14. Tsai, H. et al. High-efficiency two-dimensional Ruddlesden–Popper perovskite solar cells. *Nature* **536**, 312–316 (2016).
15. Lei, Y. et al. A fabrication process for flexible single-crystal perovskite devices. *Nature* **583**, 790–795 (2020).
16. Tsai, H. et al. Light-induced lattice expansion leads to high-efficiency perovskite solar cells. *Science* **360**, 67–70 (2018).
17. Tsai, H. et al. Design principles for electronic charge transport in solution-processed vertically stacked 2D perovskite quantum wells. *Nat. Commun.* **9**, 2130 (2018).
18. Liu, S. et al. Manipulating efficient light emission in two-dimensional perovskite crystals by pressure-induced anisotropic deformation. *Sci. Adv.* **5**, eaav9445 (2019).
19. Cheng, B. et al. Extremely reduced dielectric confinement in two-dimensional hybrid perovskites with large polar organics. *Commun. Phys.* **1**, 80 (2018).
20. Fujiwara, H. *Spectroscopic Ellipsometry: Principles and Applications* (Wiley, 2007).
21. Chatterjee, S. & Pal, A. J. Influence of metal substitution on hybrid halide perovskites: towards lead-free perovskite solar cells. *J. Mater. Chem. A* **6**, 3793–3823 (2018).
22. Abdel-Shakour, M. et al. High-efficiency tin halide perovskite solar cells: the chemistry of tin (II) compounds and their interaction with Lewis base additives during perovskite film formation. *Sol. RRL* **5**, 2000606 (2021).
23. Ruppel, W. & Wurfel, P. Upper limit for the conversion of solar energy. *IEEE Trans. Electron Devices* **27**, 877–882 (1980).
24. Ulatowski, A. M. et al. Charge-carrier trapping dynamics in bismuth-doped thin films of $MAPbBr_3$ perovskite. *J. Phys. Chem. Lett.* **11**, 3681–3688 (2020).
25. Nayak, P. K. et al. Impact of Bi^{3+} heterovalent doping in organic–inorganic metal halide perovskite crystals. *J. Am. Chem. Soc.* **140**, 574–577 (2018).
26. Li, C. et al. Highly conductive n-type $CH_3NH_3PbI_3$ single crystals doped with bismuth donors. *J. Mater. Chem. C* **8**, 3694–3704 (2020).
27. Bartolome, J. et al. Huge photostability enhancement in bismuth-doped methylammonium lead iodide hybrid perovskites by light-induced transformation. *Chem. Mater.* **31**, 3662–3671 (2019).
28. Hu, Y. et al. Bismuth incorporation stabilized α-$CsPbI_3$ for fully inorganic perovskite solar cells. *ACS Energy Lett.* **2**, 2219–2227 (2017).
29. Lyu, F. et al. Bi^{3+} doped 2D Ruddlesden–Popper organic lead halide perovskites. *J. Mater. Chem. A* **7**, 15627–15632 (2019).
30. Kruse, O., Rupprecht, J., Mussgnug, J. H., Dismukes, G. C. & Hankamer, B. Photosynthesis: a blueprint for solar energy capture and biohydrogen production technologies. *Photochem. Photobiol. Sci.* **4**, 957–970 (2005).
31. Lindholm, F. A., Fossum, J. G. & Burgess, E. L. Application of the superposition principle to solar-cell analysis. *IEEE Trans. Electron Devices* **26**, 165–171 (1979).
32. Marsen, B., Klemz, S., Unold, T. & Schock, H. W. Investigation of the sub-bandgap photoresponse in $CuGaS_2$:Fe for intermediate band solar cells. *Prog. Photovolt. Res. Appl.* **20**, 625–629 (2012).
33. Halim, M. A. Harnessing sun's energy with quantum dots based next generation solar cell. *Nanomaterials* **3**, 22–47 (2012).
34. Shockley, W. & Queisser, H. J. Detailed balance limit of efficiency of *p-n* junction solar cells. *J. Appl. Phys.* **32**, 510–519 (1961).

Article

Methods

Materials

The materials used in this study were used as purchased without further purification, which included lead iodide (PbI$_2$, 99.99%, Tokyo Chemical Industry), lead bromide (PbBr$_2$, 98%, Alfa Aesar), hydrobromic acid (HBr, 48 wt% in water, Sigma-Aldrich), methylamine (CH$_3$NH$_2$, 40% in methanol, Tokyo Chemical Industry), tin (II) oxide (SnO, 97%, Sigma-Aldrich), hydroiodic acid (57% in water, Sigma-Aldrich), hypophosphorous acid (H$_3$PO$_2$, 50 wt% in water, Sigma-Aldrich), methylammonium iodide (99.9%, GreatCell Solar), n-butylammonium iodide (99.9%, GreatCell Solar), caesium chloride (CsCl, 99.9%, Sigma-Aldrich), silver chloride (AgCl, 99%, Sigma-Aldrich), antimony (III) chloride (SbCl$_3$, 99%, Sigma-Aldrich), bismuth (III) iodide (BiI$_3$, 99%, Sigma-Aldrich), ICBA (LT-S9030, Luminescence Technology), poly[bis(4-phenyl)(2,4,6-trimethylphenyl)amine] (PTAA, LT-N168, Luminescence Technology), chlorobenzene (C$_6$H$_5$Cl, TCI America), anhydrous dimethylformamide (C$_3$H$_7$NO, 99.8%, Sigma-Aldrich), anhydrous gamma-butyrolactone (GBL, C$_4$H$_6$O$_2$, 99% Sigma-Aldrich), anhydrous dimethyl sulfoxide (C$_2$H$_6$OS, 99.9%, Sigma-Aldrich), isopropanol (IPA, C$_3$H$_8$O, 99.5%, Sigma-Aldrich) and methanol (99.8%, CH$_3$OH, Sigma-Aldrich).

Preparation of single-crystal perovskites

MAPbBr$_3$: flat and smooth centimetre-sized bulk MAPbBr$_3$ single crystals were prepared by solution-based growth[35]. The single crystal was used as the 3D perovskite substrate to grow the low-dimensional perovskite superlattice without any further treatment. MAPbI$_3$: MAPbI$_3$ single crystals were prepared by solution-based growth[15]. The as-obtained crystals were ultrasonically cleaned in an anhydrous IPA solvent for 5 min. Then the crystals were crushed into powders for growth precursor preparation.

Synthesis of low-dimensional perovskites

7.5 mmol SnO was added into 10 ml steaming hydroiodic acid (57 wt%) mixed with 2.5 ml H$_3$PO$_2$ (50 wt%) aqueous solution until the precursor solution become transparent yellow. Then the stoichiometric n-butylammonium iodide (3 mmol)/methylammonium iodide (6 mmol) methanol solution was injected into the precursor solution under stirring. Later, the beaker was transferred into a vacuum chamber to remove the dissolved oxygen and left standing for crystallization. Crystal flakes would appear after around 2 h. Then IPA was used to wash the crystals three times. Finally, the crystals were dried in vacuum and then directly dissolved in GBL to form the growth solution (0.5 M) for low-dimensional perovskites. For the Bi^{3+}-alloyed superlattice, 10% molar ratio of BiI$_3$ was dissolved into the growth solution under room temperature. The solution was filtered before use to remove any undissolved components.

Preparation of precursors for mixed and double perovskites

The mixed perovskite MAPb$_{0.5}$Sn$_{0.5}$Br$_3$ was prepared by mixing MABr, PbBr$_2$ and SnBr$_2$ with a 2:1:1 molar ratio in dimethylformamide (1.5 M). The double perovskite Cs$_2$AgSbCl$_6$ precursor solution was prepared by directly mixing CsCl, AgCl and SbCl$_3$ with a 2:1:1 molar ratio in dimethyl sulfoxide (0.4 M). The as-prepared solution was stirred at 60 °C until the solution became clear. Then adding 0.4 M MAPbI$_3$ single-crystal powder to the solution completed precursor solution preparation for achieving a suitable lattice constant with minimal lattice mismatch between the substrate and the inorganic slab of the epitaxial layer.

Device fabrication

MAPbBr$_3$ bulk crystals were used as the 3D substrates as their synthesis is well established. To further reduce the lattice mismatch, the mixed perovskite (or double perovskite) precursor was hot casted onto the MAPbBr$_3$ crystal to form a smooth epitaxial layer, which was the actual substrate surface for growing the low-dimensional perovskites. The thickness of the smooth epitaxial layer did not influence the subsequent superlattice growth or device fabrication. Polyimide films (12.7 μm thick) were prepatterned (with an opening size of 1 μm × 1 μm) to serve as the growth mask by following a reported method[15]. Then a layer of Au was deposited by sputtering to serve as the bottom electrode. Later, PTAA solution (1.5 mg ml^{-1} in anhydrous toluene) was directly spin-coated onto the patterned polyimide/Au films at 2,500 rpm for 30 s, followed by annealing at 80 °C for 3 min. Then the growth substrate was laminated with the polyimide/Au/PTAA mask and then spin-coated by supersaturated mixed perovskite (or double perovskite) precursor at 4,000 rpm for 30 s, followed by annealing at 100 °C for 5 min. Subsequently, low-dimensional perovskite growth solution (0.5 M in GBL) was spin-coated on the substrate at 1,500 rpm for 60 s, followed by annealing at 180 °C for 2 min to form the superlattice absorber layer. After that, ICBA (20 mg ml^{-1} in chlorobenzene) was spin-coated onto the epitaxial layer, followed by annealing at 100 °C for 5 min. Finally, a layer of ITO was deposited by sputtering to serve as the transparent top electrode. The polycrystalline devices are fabricated by hot casting[22].

DFT calculations

First-principles DFT calculations were performed using the Vienna Ab initio Simulation Package[36]. The projector augmented-wave pseudopotential was used for describing electron–ion interactions[37]. The generalized gradient approximation parameterized by Perdew, Burke and Ernzerhof was used to treat the electron–electron exchange-correlation functional[38]. The van der Waals functional DFT-D3 was applied to properly describe the long-range dispersion interactions between the organic molecules in the hybrid materials[39]. The hybrid functionals within Heyd–Scuseria–Ernzerhof formalism with 70% Hartree–Fock exchange were used to calculate bandgaps for the Sn-based perovskites[40,41]. The wave functions were expanded in a plane-wave basis set with a cut-off energy of 400 eV. The structures for conventionally grown single-crystal Ruddlesden–Popper perovskites and epitaxially grown perovskites were built on the basis of experimental results of the lattices. The atomic positions were fully optimized until all components of the residual forces were smaller than 0.03 eV Å^{-1}. The convergence threshold for self-consistent field iteration was set at 10^{-5} eV. Γ-centred $2 \times 1 \times 4$ and $4 \times 4 \times 1$ k-point grids were used for superlattice and conventionally grown single crystals, respectively. Owing to the limited computational resources, we could only simulate the $n = 3$ structure, but this would not influence the device ($n = 5$) because the formation mechanism of the double-bandgap structure was the same.

Morphology characterization

All SEM images were taken using a Zeiss Sigma 500 microscope. All optical images were taken using a Zeiss Axio Imager optical microscope.

Structure characterization

X-ray diffraction was measured by a Rigaku 393 Smart lab diffractometer equipped with a Cu Kα1 radiation source ($\lambda = 0.15406$ nm) and a Ge 394 (220 × 2) monochromator. The STEM images were taken using a cryo-FEI 200 kV Sphera microscope. Samples for the STEM were prepared using a frozen focused ion beam (FEI Scios DualBeam FIB/SEM). The conventionally grown single crystal was hard to be imaged by STEM because the sample without an epitaxial substrate curled quickly owing to its instability in the scanning transmission electron microscope. X-ray photoelectron spectroscopy measurements were carried out using Kratos AXIS Supra with a He I (21.22 eV) source under 10^{-8} torr chamber pressure.

Optical characterizations

Photoluminescence and time-resolved photoluminescence measurements were performed with a confocal microscope system by focusing a monochromatic 6-ps pulsed laser with a 4× objective lens (numerical

aperture 0.13). Optical functions were measured by ellipsometry (J.A. Woollam M-2000D spectroscopic ellipsometer). Ultraviolet photoelectron spectroscopy measurements were carried out using Kratos AXIS Supra with a He I (21.22 eV) source under 10^{-8} torr chamber pressure. Ultraviolet–visible spectroscopy and absorption spectra were collected using a PerkinElmer Lambda 1050 ultraviolet–visible spectroscopy system under the reflection mode.

Electrical characterizations

Polarized photocurrent was measured with a polarizer. Time of flight was measured by extracting the decay time of the transient photocurrent to calculate the carrier mobility. An external bias of 0.5 V was used to power the devices with a resistor connected in series. Orientation-dependent transient photovoltages were measured with an oscilloscope (Agilent MSO6104A Channel Mixed Signal) to study the carrier lifetime. A pulsed laser with a pulse width of less than 10^{-10} s was used as the light source. The EBIC was collected using a FEI Scios DualBeam microscope with a Mighty EBIC 2.0 controller (Ephemeron Labs) and a Femto DLPCA-200 preamplifier. Lateral Au electrodes were deposited by electron-beam evaporation for surface measurements; a prepatterned Au-coated polyimide film was used as the bottom electrode for cross-section measurements; the top surface was deposited with a layer of Au by electron-beam evaporation to serve as the top electrode. The EBIC and SEM images of the same region of interest were collected simultaneously. The samples were several micrometres in thickness, whereas EBIC could penetrate up to several micrometres into the samples[42]. The transient absorption spectroscopy was performed using an ultrafast transient absorption system with a tunable pump and white-light probe to measure the differential absorption through the sample. The laser system consisted of a regeneratively amplified Ti:sapphire oscillator (Coherent Libra), which delivered 4-mJ pulse energies centred at 800 nm with a 1-kHz repetition rate. The pulse duration of the amplified pulse was approximately 50 fs. The laser output was split by an optical wedge to produce the pump and probe beams and the pump beam wavelength was tuned by an optical parametric amplifier (Coherent OPerA). The pump beam was focused onto the sample by a spherical lens at near-normal incidence (spot size of full width at half maximum (FWHM) about 300 μm). The probe beam was focused onto a sapphire plate to generate a white-light continuum probe, which was collected and refocused onto the sample by a spherical mirror (spot size of FWHM approximately 150 μm). The transmitted white light was collected and analysed with a commercial absorption spectrometer (HELIOS, Ultrafast Systems LLC). Pulse-to-pulse fluctuations of the white-light continuum were accounted for by a simultaneous reference measurement of the continuum. The pump wavelength was maintained at 610 nm with a pulse power of 100 nJ (or approximately 80 μJ cm^{-2}). The pump and probe beams were linearly cross-polarized and any scattered pump light into the detection path was filtered by a linear polarizer. The time delay was adjusted by delaying the pump pulse with a linear translation stage (minimum step size 16 fs). The individual component kinetic traces were fit to biexponential decays by least squares means.

Photovoltaic characterizations

J–V measurements were carried out using a Keithley 2400 source meter under a simulated air mass of 1.5 irradiation (100 mW cm^{-2}) and a xenon-lamp-based solar simulator (Oriel LCS-100). Temperature-dependent J–V measurements were performed with the sample in a liquid-nitrogen-cooled metal tank, in which one side was glass to allow illumination. The same configuration was used for both epitaxial and polycrystalline devices. EQE data were collected by illuminating the device under monochromatic light using a tungsten source (chopped at 150 Hz) while collecting the photocurrent by a lock-in amplifier in the alternating current mode. The 2D mapping of the thickness-dependent EQE was generated from the Contour-Color Fill function. Wavelength-dependent J–V measurements were carried out by applying a series of bandpass filters (FWHM about 150 nm) under the solar simulator to measure both the polycrystalline and epitaxial devices.

Data availability

All data are available in the manuscript or supplementary materials.

35. Lei, Y. et al. Controlled homoepitaxial growth of hybrid perovskites. *Adv. Mater.* **30**, 1705992 (2018).
36. Kresse, G. & Furthmüller, J. Efficient iterative schemes for *ab initio* total-energy calculations using a plane-wave basis set. *Phys. Rev. B* **54**, 11169 (1996).
37. Blöchl, P. E. Projector augmented-wave method. *Phys. Rev. B* **50**, 17953 (1994).
38. Perdew, J. P., Burke, K. & Ernzerhof, M. Generalized gradient approximation made simple. *Phys. Rev. Lett.* **77**, 3865 (1996).
39. Grimme, S., Antony, J., Ehrlich, S. & Krieg, H. A consistent and accurate *ab initio* parametrization of density functional dispersion correction (DFT-D) for the 94 elements H-Pu. *J. Chem. Phys.* **132**, 154104 (2010).
40. Heyd, J., Scuseria, G. E. & Ernzerhof, M. Hybrid functionals based on a screened Coulomb potential. *J. Chem. Phys.* **118**, 8207–8215 (2003).
41. Yang, D. et al. Functionality-directed screening of Pb-free hybrid organic–inorganic perovskites with desired intrinsic photovoltaic functionalities. *Chem. Mater.* **29**, 524–538 (2017).
42. Powell, K. M. & Yoon, H. P. Depth-dependent EBIC microscopy of radial-junction Si micropillar arrays. *Appl. Microsc.* **50**, 17 (2020).

Author contributions S.X. and Y. Lei conceived the idea. Y. Li carried out the DFT calculations. Y. Lei, C.L. and R.W. synthesized the materials, prepared the substrates and fabricated the devices. Y. Lei, Q.Y., S.Z., H.G. and Y.C. contributed to the structural characterizations. S.Z. contributed to the grazing-incidence wide-angle X-ray scattering characterizations. F.B. and Y.W. contributed to the transient absorption spectroscopy characterizations. J.Z. contributed to the optical and electrical characterizations. R.Z. carried out the Fourier transform infrared spectroscopy characterizations and the simulations. All authors contributed to analysing the data and commenting on the manuscript.